Live imaging and modeling of inner nuclear membrane targeting reveals its molecular requirements in mammalian cells

Andrea Boni, Antonio Z. Politi, Petr Strnad, Wanqing Xiang, M. Julius Hossain, and Jan Ellenberg

Cell Biology and Biophysics Unit, European Molecular Biology Laboratory, Heidelberg 69117, Germany

Targeting of inner nuclear membrane (INM) proteins is essential for nuclear architecture and function, yet its mechanism remains poorly understood. Here, we established a new reporter that allows real-time imaging of membrane protein transport from the ER to the INM using Lamin B receptor and Lap2β as model INM proteins. These reporters allowed us to characterize the kinetics of INM targeting and establish a mathematical model of this process and enabled us to probe its molecular requirements in an RNA interference screen of 96 candidate genes. Modeling of the phenotypes of genes involved in transport of these INM proteins predicted that it critically depended on the number and permeability of nuclear pores and the availability of nuclear binding sites, but was unaffected by depletion of most transport receptors. These predictions were confirmed with targeted validation experiments on the functional requirements of nucleoporins and nuclear lamins. Collectively, our data support a diffusion retention model of INM protein transport in mammalian cells.

Introduction

The nuclear envelope (NE) consists of two lipid bilayers, the outer nuclear membrane (ONM) in continuity with the ER and the inner nuclear membrane (INM) facing the nucleoplasm, which are connected at each nuclear pore complex (NPC). The INM is a highly specialized membrane compartment with many resident integral membrane proteins that have key functions in nuclear architecture such as linking the INM with chromatin and the nuclear lamina intermediate filament meshwork, transcription regulation, and signal transduction (Gomez-Cavazos and Hetzer, 2012). Cycling cells have to double the surface of the NE in interphase to maintain homeostasis for the next division, which requires constant targeting of INM proteins (Burke and Stewart, 2006). Despite the importance of delivering INM proteins, their targeting mechanism is poorly understood.

Newly synthesized INM proteins are inserted into the ER membrane from where they move laterally by diffusion through ER cisternae and tubules to the ONM. A key mechanistically controversial step is INM protein translocation from the ONM to the INM at the NPC, for which different models have been proposed depending on the type of INM protein and organism studied. In the diffusion retention model, the translocation between the ONM and INM is believed to occur by undirected passive diffusion through a narrow ~10-nm-diameter peripheral channel between the NPC and nuclear membrane (Reichelt et al., 1990; Beck et al., 2004). This peripheral channel would impose a size constraint on the cytoplasmic domain of INM proteins (Soullam and Worman, 1995; Theerthagiri et al., 2010; Antonin et al., 2011). Enrichment in the INM over the ER/ONM then occurs by interaction with nuclear binding partners such as lamins or chromatin, which would be required to retain INM proteins in the nucleus. This model has been supported by early studies on different INM proteins (Powell and Burke, 1990; Smith and Blobel, 1993; Soullam and Worman, 1995; Ellenberg et al., 1997; Yang et al., 1997) and does not require active or receptor-mediated translocation of INM proteins across the NPC.

More recent studies have suggested a different model, termed receptor-mediated translocation in analogy to the well characterized transport mechanism of soluble proteins (King et al., 2006; Meinema et al., 2011). This model is mostly based on studies on the yeast INM proteins Heh1p and Heh2p, which require a functional RanGTPase system as well as importin α and β1 for the INM protein targeting process (King et al., 2006; Meinema et al., 2011). Here, translocation is believed to involve the cytoplasmic domain of INM proteins to reach into the central channel of the NPC, implying a continuous open path for membrane proteins through the walls of the NPC channel (Meinema et al., 2011). A variant of this model, based on the yeast protein Mps3, proposed that INM proteins bind to soluble import substrates

The Rockefeller University Press $30.00
J. Cell Biol. Vol. 209 No. 5   705–720
www.jcb.org/cgi/doi/10.1083/jcb.201409133

JCB   705

and "piggyback" on their transport receptor–mediated nuclear import (Gardner et al., 2011). In addition to the work in yeast, also for some mammalian INM proteins an energy and/or RanGTP requirement has been described for targeting. It has been shown that targeting of an INM reporter is impaired by ATP depletion (Ohba et al., 2004) and more recently a systematic study of several INM proteins proposed requirements for ATP and/or the RanGTPase system (Zuleger et al., 2011). The conservation of nuclear localization signals in many mammalian INM proteins has been taken as additional support for the receptor-mediated translocation model (Lusk et al., 2007). However, their functional requirement and mechanistic contribution to the INM protein targeting process, e.g., whether they may function in translocation or retention, remains controversial (Turgay et al., 2010). In addition, a sorting motif (INM-SM) consisting of positively charged amino acids has been found in several INM proteins (Braunagel et al., 2004; Saksena et al., 2004). INM-SM is recognized by a short isoform of importin α that has been proposed to promote accumulation of INM proteins at the ONM as well as translocation through the NPC (Saksena et al., 2006; Braunagel et al., 2007, 2009).

Progress in the field is currently hampered by the absence of suitable tools for an unbiased assessment of the molecular requirements for INM protein targeting. Furthermore, most of the evidence for the receptor-mediated transport model has come from the yeast model system, which has a very specialized nuclear architecture and it remains less clear to what extent these findings apply to mammalian cells. To address this, we have developed an INM protein targeting reporter system for live imaging in mammalian cells that allows the acute release of a large pool of fluorescently tagged INM proteins from the ER by a self-cleaving retention domain, enabling us to quantitatively assay the kinetics of the transport process to the INM. We first applied this system to Lamin B receptor (LBR), a well characterized INM protein containing functional domains that bind to B-type lamins, heterochromatin protein 1 (HP1), and histone H3/H4, consistent with a diffusion retention model, as well as three nuclear localization signals, consistent with receptor-mediated translocation. Exploiting this reporter, we screened 96 candidate genes for their requirement in LBR reporter targeting by siRNA knockdown (KD) and automated high resolution confocal time-lapse microscopy. These genes include nucleoporins, importins, and lamins as well as NE and ER membrane proteins. Using a mathematical model of the INM protein-targeting process, we could fit the kinetic signatures of the different transport phenotypes and cluster the scoring genes into three major phenotypic classes, predicted to be required for controlling the number of NPCs, their permeability, and the strength of nuclear retention, which we could validate with targeted mechanistic experiments. To test if these findings are valid beyond the LBR-based reporter, we extended our strategy to the INM protein Lap2β and retested genes of the major phenotypic categories identified with LBR. We find that the Lap2β reporter recapitulates the transport phenotypes seen for LBR, but uses a different nuclear retention mechanism. Overall, our data are consistent with diffusion retention as the predominant mechanism for targeting of LBR- and LAP2β-type INM proteins in mammalian cells and do not provide strong evidence for a receptor-mediated transport model.

Results

Target-INM: a reporter to visualize INM protein targeting in live cells

To follow INM protein trafficking between the ER and INM in live cells we developed an inducible reporter system (Target-INM; Fig. 1 A). It was shown previously that adding the 60-kD chicken muscle pyruvate kinase (CMPK) domain to the N terminus of the LBR prevents its targeting to the INM and leads to its retention in the ER (Soullam and Worman, 1995). We therefore placed a retention domain composed of the hepatitis C virus (HCV) NS3 protease, the CMPK domain, and an NS3 cleavage site in front of the N terminus of a minimal LBR construct (N terminus and the first transmembrane domain followed by GFP; Ellenberg et al., 1997; Fig. 1 A). In a HeLa cell line expressing this reporter, the NS3 protease (Lin et al., 2008) could then be acutely induced by washout of its inhibitor BILN2061 (Lamarre et al., 2003). NS3 protease activation leads to removal of the retention domain (Fig. 1 B) and relocalization of the reporter from the ER to the NE (Fig. 1 C). That NE signal corresponded to INM localization of the reporter was confirmed by its reduced mobility measured by FRAP after protease induction compared with the reporter mobility in the ER before protease activation (Fig. S1 A) and immunostaining after differential permeabilization of the plasma membrane with digitonin of the reporter carrying a Myc tag in the nucleoplasmic domain (Fig. S1 B). For the rest of the text we refer to the LBR-based reporter as Target-INM-LBR.

A high throughput assay for INM protein targeting

Having validated the Target-INM-LBR reporter, we next set up a high throughput quantitative imaging assay to identify genes implicated in INM protein targeting by RNAi screening. To this end, the Target-INM-LBR cell line was seeded on custom spotted siRNA microarrays (Neumann et al., 2010); after 24 h, reporter expression was induced by doxycycline addition and after 48 h automatic confocal time-lapse imaging of reporter localization before and after cleavage induced by protease inhibitor washout was performed (Fig. 2 A). The resulting 2.5-h movies of Target-INM-LBR translocation after gene KD were analyzed using CellCognition (http://www.cellcognition.org) to segment and track cells based on the nuclear marker H2B-mCherry (Held et al., 2010; Walter et al., 2010), selecting cell trajectories that remained in interphase for the entire movie (Fig. 2 C). To quantify INM protein targeting we developed an image analysis pipeline that automatically detects in-focus NE and adjacent ER regions to measure the fluorescence intensity in both compartments over time (Fig. 2 D and Fig. S2 A). Single cells growing on scrambled control siRNA array spots showed that, after cleavage, the reporter intensity increased in the NE with the corresponding decay in the ER (Fig. 2 E). As a simple score for maximal reporter accumulation in the NE we defined the parameter NE increase (fold change; Fig. 2 E), a reliable and reproducible indicator of reporter accumulation in ~50 cells of a single siRNA microarray replicate (Fig. 2 F), which was narrowly distributed across the whole screen (Fig. 2 G) and was independent of the reporter expression level (Fig. S2 C).

Identification of genes implicated in INM protein targeting

The high temporal resolution of our assay provides high sensitivity and can score kinetic phenotypes, with a throughput
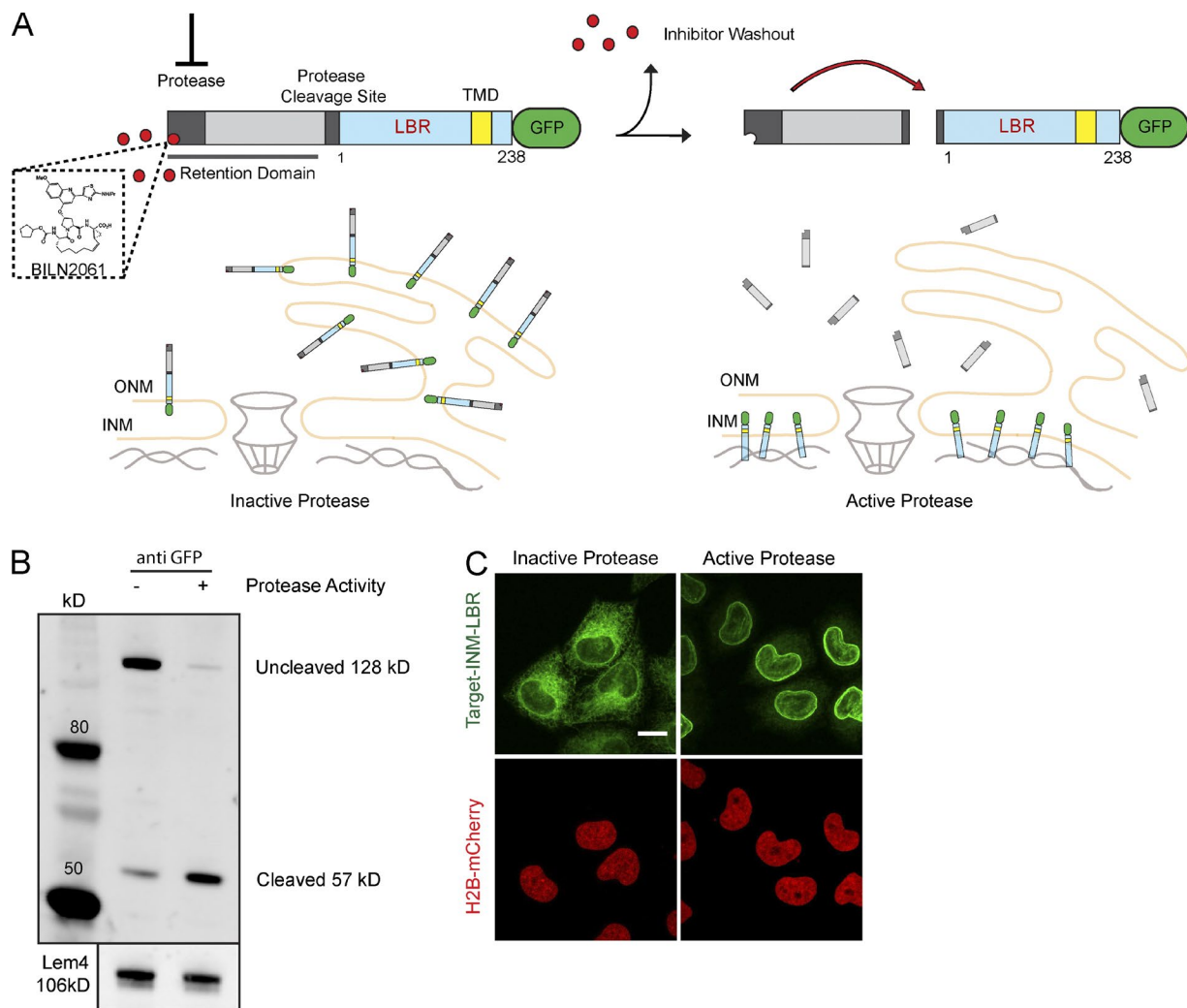
Figure 1. **Target-INM: an inducible reporter for INM protein targeting.** (A) Schematic representation of the LBR-based reporter and its predicted subcellular localization before (left) and after (right) protease activation by inhibitor washout. In gray is the retention domain consisting of the NS3 protease, the protease cleavage site (dark gray), and CMPK domain (light gray). LBR 1–238 containing the N-terminal domain (light blue) and first transmembrane domain (TMD) (yellow) followed by GFP is shown. (B) Western blot of cells grown for 24 h in the presence (protease activity –) or absence (protease activity +) of the protease inhibitor. The ER retention domain is fully cleaved in cells with active protease. (C) Confocal images of HeLa cells stably expressing H2B-mCherry and Target-INM-LBR grown for 24 h in the presence (inactive protease) or absence (active protease) of the protease inhibitor BILN2061. Bar, 10 µm.

of 26 siRNAs per microarray. We therefore selected 96 candidate genes, likely to be required for INM protein targeting, which can be divided into the following functional groups: (1) nucleoporins, (2) validated INM proteins, (3) nuclear binding partners of INM proteins, (4) ER remodeling proteins, and (5) nucleocytoplasmic transport factors (Table S3). After screening of 73 microarrays with two independent siRNAs per gene in three to four replicates resulting in 2,200 time-lapse movies, siRNAs where ranked by their mean deviation in NE increase from control siRNAs (Fig. 3 A, marked blue if at least two of the three to four microarray replicates deviated significantly; and Table S4). A gene was scored as a high confidence hit when two independent siRNAs targeting the same gene showed a reproducible effect (Fig. 3 A, gene names). We found that most high confidence hits reduced NE accumulation of the reporter, while one gene also increased targeting. The vast majority of gene hits required for INM protein targeting are nucleoporins, whose depletion decreased NE accumulation. Almost all components of the Nup107–160 complex showed a

consistent phenotype with a 50–80% lower NE increase compared with control siRNA (Fig. 3, A and C). We also observed a similar effect for Nups that do not belong to the Nup107–160 complex as for NUP153 and NUP93 KDs (Fig. 3, A and D). In addition, depletion of two proteins, the ONM protein Nesprin-1 (SYNE1) and the transmembrane nucleoporin Ndc1 (TMEM48), caused a milder but significant and reproducible reduction of reporter accumulation. Lamin A depletion dramatically increased reporter accumulation with an 80% higher NE increase than control siRNA (Fig. 3, A and B). Although we targeted the complete set of importins with siRNAs, none of these depletions affected reporter accumulation except for a mild reduction in reporter accumulation after importin β1 (KPNB1) KD. Inspecting the time-lapse images of single cell trajectories revealed two different underlying phenotypes for genes that scored with a lowered NE increase. For the large majority of these genes, including most of the nucleoporins, the reporter did not show any significant accumulation at the INM over its levels in the ER, which is consistent with impair-
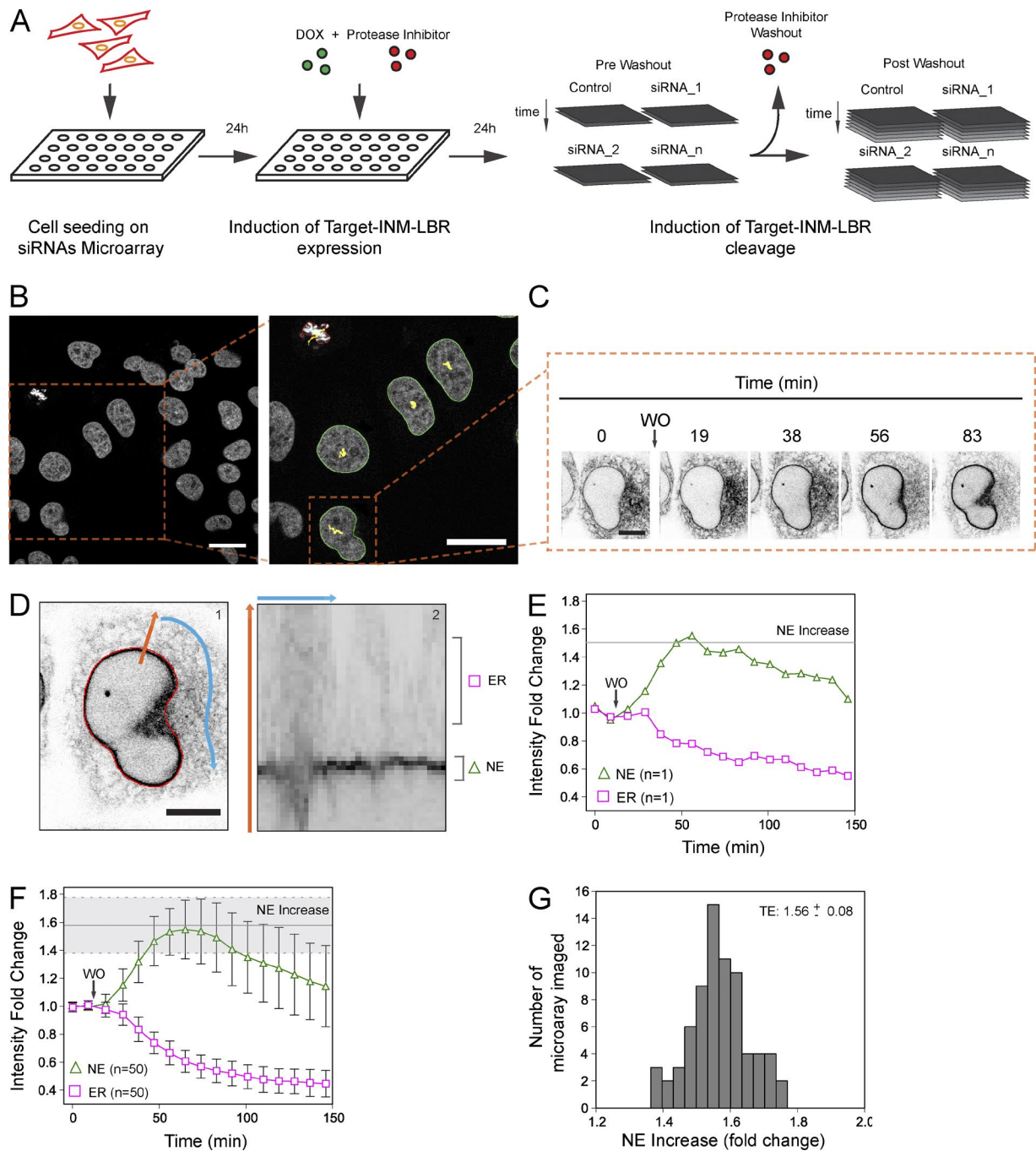
Figure 2. **Target-INM-LBR–based screening pipeline.** (A) Schematic representation of screening workflow. Each siRNA microarray was generated by siRNA spotting as described in Erfle et al. (2008). Cells were seeded on the microarray and, after 24 h, Target-INM-LBR expression is induced by adding Doxycycline (1 µg/ml) together with the protease inhibitor BILN2061 (2 µM). After an additional 24 h, i.e., 48 h of siRNA treatment, imaging is started. Each siRNA position is imaged before and after inhibitor washout for in total 2.5 h. (B) Representative field of view of images acquired in the screening setup showing H2B-mCherry signal. The zoomed inset shows segmentation, tracking, and cell classification of interphase (green) and mitotic (red) cells based on CellCognition software. Bars, 25 µm. (C) Example of a single interphase cell trajectory. The images show translocation of the reporter to the INM after inhibitor washout. Bar, 10 µm. (D) Image analysis workflow. (1, left) The boundary of the segmented H2b-mCherry signal (red line) seeds a domain in the nucleus-to-ER direction (orange arrow) around the surface of the nucleus (blue arrow). Bar, 10 µm. (2, right) This domain is unfolded along the blue arrow, and the regions for measuring NE (green triangle) and ER intensities (magenta rectangle) are determined (see also Fig. S2 A). (E) Quantification of a single cell trajectory. The plot shows intensity fold change of the NE and ER normalized to the mean of the first two pre-washout time points. Gray line is the NE increase (fold change) defined as the mean of the NE's three highest consecutive values. (F) Quantification of control siRNA NE and ER fold changes in a single replicate of the screening (time points are mean ± SD). The gray line is the replicate mean NE increase (fold change; region within SD is indicated by the gray area). (G) Distribution of mean NE increase (fold change) of control siRNA across all the microarrays imaged (*n* = 73).

ment in translocation to and/or retention in the INM, as exemplified by SEC13 KD (Fig. 3 C). In contrast to all the other genes in NUP93 KD, the full-length reporter accumulated at

the INM already before inhibitor washout, suggesting a loss of size selectivity of INM targeting (Fig. 3 D). Therefore, the lower NE increase scored for NUP93 KD can be attributed to

the absence in the ER of a "ready-to-translocate" pool of the full-length reporter rather than an impairment of translocation.

A kinetic model to predict the mechanism underlying INM protein targeting phenotypes

Although we used a single parameter to identify genes implicated in INM protein targeting, our screening data contains detailed kinetic information for each hit. To exploit this information and gain insight into the mechanism underlying the siRNA phenotypes we developed a mathematical model for INM protein targeting between the ER and INM (Fig. 4 A and Materials and methods). The model is used to describe the change in reporter concentration in the ER and the NE (sum of INM and ONM mean intensity). We model production, cleavage, and degradation of the reporter, as well as import and export of the cleaved reporter, through the nuclear pore, with the import rate constant k_i and the effective export rate constant k_o, respectively. The magnitude of both transport rate constants is proportional to the pore permeability and the number of pores (Eqs. 1 and 2). We did not explicitly model the exchange between ER and ONM because the ER diffusion of the reporter is fast compared with its cleavage and translocation (Fig. S1 A) and therefore assumed that the ONM reporter concentration equals that of the ER. Using the FRAP (Fig. S1 A) and targeting kinetics (Fig. 4 B) we estimated that the binding time of the reporter to nuclear interactors is between 0 and 4 min (see Materials and methods). Under these conditions an effective export rate constant k_o, proportional to the unbound fraction of the reporter in the INM, can be used to approximate the binding to nuclear interactors (see Materials and methods for further details and Eq. 2). These assumptions were further validated by the fact that explicitly including ER-ONM exchange or nuclear binding did not significantly improve the model fits to the data (F-test, P > 0.1). To account for the known size selectivity of the pore, we introduced the fitting parameter λ that reduces both import and export rates for the uncleaved reporter. After washout of the inhibitor, the NE intensity fold change shows a transient maximum and then decreases. This behavior could be caused by photobleaching or a decreased stability of the reporter after cleavage. We could rule out photobleaching under the low light imaging conditions used (unpublished data) and therefore model two different degradation rate constants, d_F and d_C, for the full-length and cleaved forms of the reporter. For LBR, we could not find a significant difference between degradation of the cleaved form in the INM or in the ER, therefore $d_{CINM} = d_C$.

We first used the model to determine the set of rate constants characterizing the reporter targeting in control conditions without gene silencing. The cleavage rate constant k_c was determined by assaying the protease cleavage kinetics (Fig. S3, A and B) and the surface ratio of nuclear-to-ER membrane was determined from high resolution 3D images of the whole cell reporter distribution (Fig. S3 C). In the model, the translocation kinetics from ER to INM does not depend on the exact value of reporter production rate, which is consistent with the absence of a correlation of the initial ER intensity and the maximal NE intensity reached during translocation (Fig. S2 C), and we therefore fixed production to a constant value for the 2.5-h observation time. The remaining rate constants were estimated by fitting the model to experimental data for changes in NE and ER reporter density after cleavage induction and the initial NE-to-ER density ratio (Fig. 4 B). As expected, the transient peak

in NE fold increase could be explained by reduced protein stability after cleavage (approximately threefold reduced lifetime). Thus the model predicts that after washout of the inhibitor the total amount of protein decreases, a prediction that we could confirm experimentally (Fig. S3 D). We found that the transport through the nuclear pore is in the order of minutes for the cleaved form and negligible for the uncleaved. The transport from the ER to the INM has a characteristic time of $t_{1/2} = \log(2)/k_i = 3.6$–$5.4$ min, whereas the inverse process, returning to the ER from the INM, is about five times slower with a characteristic time $t_{1/2} = \log(2)/k_o = 18.3$–$25.6$ min. This slow export can be accounted for by the binding to the INM, with an estimated bound fraction of 0.78–0.8 (Eq. 3).

The model predicts three major control mechanisms for INM protein targeting

To test if our model made accurate predictions, we used a mutated version of the reporter for which the mechanism behind the targeting defect is known, Target-INM-Δ60LBR, a construct which lacks the lamin B and chromatin binding domains of LBR required for nuclear retention, but still contains its nuclear localization signals that may act in receptor-mediated transport (Fig. S3 F; Ye and Worman, 1994). To determine which rates are affected in the Target-INM-Δ60LBR reporter, we fitted combinations of one or more parameters to the NE and ER kinetics while leaving the other model parameters unchanged from the reference values obtained with full-length Target-INM-LBR. Combinations with more than one parameter were considered only if they yielded significantly better fits (Kolmogorov-Smirnov test, P < 0.01; Fig. S3, G and H). Similarly, an asymmetric change in transport (e.g., a change of only import or export rate) was only considered if it yielded a significantly better fit than a symmetric change (i.e., the same change of both rates). For further details see Materials and methods.

As expected for a reporter unable to interact with nuclear binding partners, the model predicted an 8.5-fold increase in effective export rate k_o, suggesting that nuclear retention is severely affected (Fig. S3, G and H). Because our model could predict the mechanism underlying the Target-INM-Δ60LBR targeting defect, we next used it to analyze the new phenotypes observed for the hits in our RNAi screen.

The model was able to obtain good fits for all siRNAs (goodness of fit $R_2 > 0.97$) experiments targeting high confidence hit genes (e.g., Fig. 4 C). Using the same strategy to obtain the minimal number of parameter changes required for an optimal fit, we clustered the genes according to the type of parameters that differed from nonsilencing control experiments and ranked them in each cluster by the magnitude of the difference. The model distinguished three classes of genes (Fig. 4 D). In the first cluster (Fig. 4 D, a) containing 12/15 of the genes, the model showed that an equal change in both import and export rate constants was sufficient to obtain a good fit, which for 11 genes was a transport rate reduction, suggesting a decrease in the number of pores and/or their permeability. For some genes in cluster a, the model additionally predicted a decrease in stability of the cleaved reporter. For cluster b, the model predicted a selective effect on the export rate from nucleus to cytoplasm, whereas import was predicted to be unchanged. Finally, for cluster c, containing all siRNAs for NUP93, the model predicts an increase in pore permeability for the uncleaved reporter and thus a decrease in size selectivity of the pore. The change of this parameter accounted for the observed precleavage accu-

Figure 3. **Screening hits.** (A) siRNAs ranking based on the mean deviation of the NE increase (fold change) from control siRNA. Blue bars indicate siRNAs that deviate from control siRNA with statistical significance in at least two replicates. siRNAs on the left of control siRNA show an increase, whereas those on the right show a decrease of NE increase (fold change) with respect to control siRNA. Labels indicate hit genes for which both siRNAs show a reproducible effect. The lines are pointing to the siRNA that shows the stronger effect. (B–D) Representative single cell trajectory images for the three main phenotypic classes: LMNA KD (B), SEC13 KD (C), and NUP93 KD (D) cells. Bars, 10 μm. The plots show NE fold change for the control siRNA (gray triangle) and for the indicated gene KD (green triangle). Error bars for the genes KD show the SD of the mean. KD efficiency is shown in Fig. S2 B.
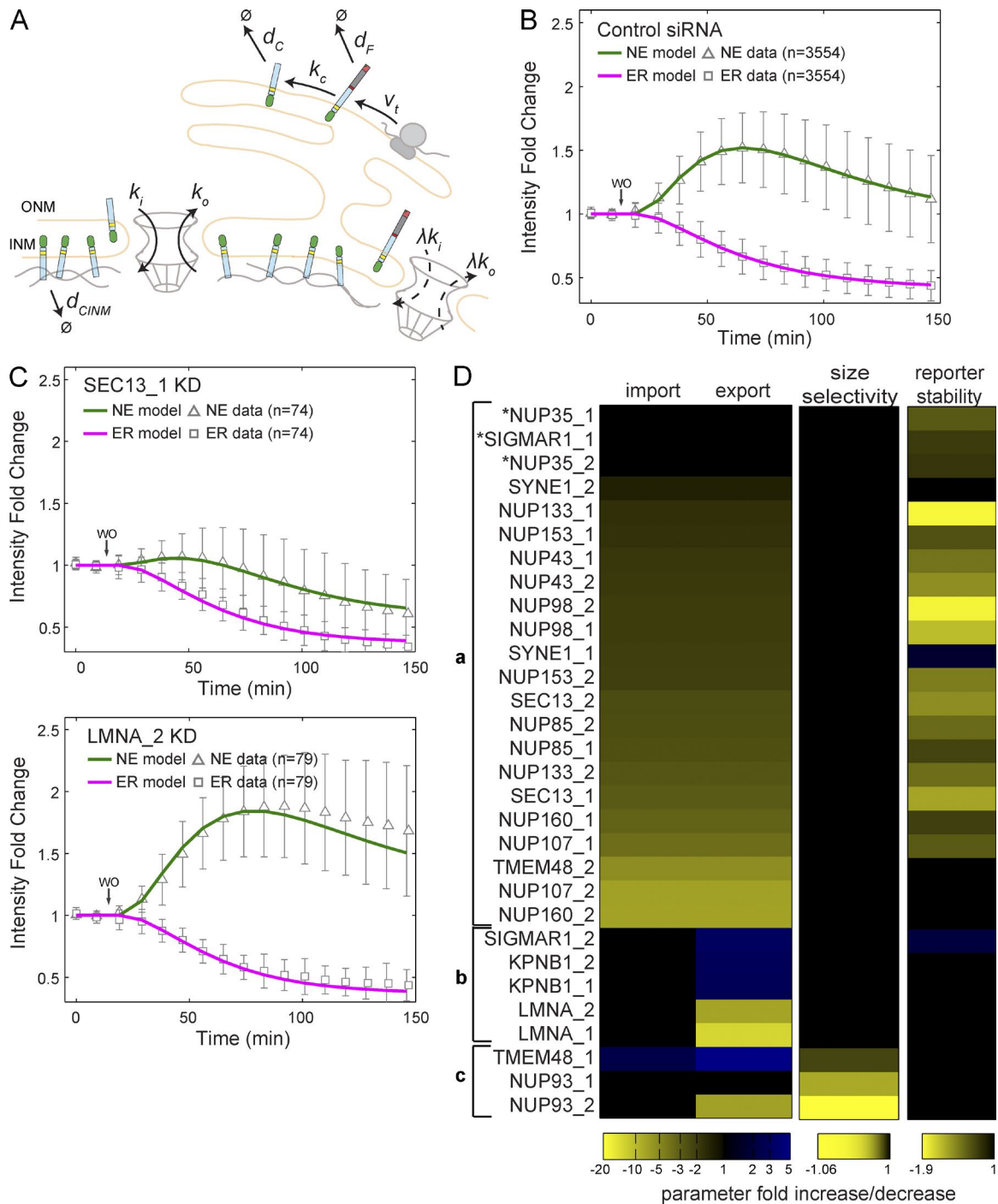
Figure 4. **Model for nuclear translocation of INM proteins.** (A) Schematic representation of the mathematical model. The model has two compartments, the ER and the INM, with the membrane area ratio $\alpha = A_{ER}/A_{NE}$. The model accounts for translation (v_t), degradation of the reporter construct (d_C, d_{CINM}, and d_F), and the cleavage of the ER retention domain (k_c). The translocation of the reporter to the INM is set by the import and export rate constants (k_i and k_o, respectively). The uncleaved protein can be transported with reduced rates set by λ. (B) The reference parameter set is obtained by fitting the model (solid lines) to all cell trajectories for control siRNA from 73 microarrays (symbols). Error bars are the SD of the mean. For estimated parameters, see Table S1. (C) Example fits for SEC13 KD and LMNA KD. Error bars for the genes KD show the SD of the mean. For estimated parameters, see Table S1. (D) Parameter fold changes with respect to the reference set for each of the two siRNAs of the 15 hit genes. Cells from each siRNA replicate have been pooled. The cleaved reporter stability is defined by $1/d_C$, the size selectivity is $1 - \lambda$. For three siRNAs (asterisks) a fit to the data could also be obtained by varying the reporter stability of the cleaved form only.

mulation of the full-length reporter in the NE and the reduced targeting after inhibitor washout (Fig. 3 D).

Experimental validation shows that fewer pores, stronger nuclear retention, and loss of size selectivity explain the targeting phenotypes

For most of the high confidence hits in clusters a our model predicted both import and export rate constants to be concomitantly reduced. Because these rates are proportional to the number of pores and/or pore permeability (Eqs. 1 and 2) and almost all these hits are nucleoporins, this phenotypic class could be caused by a decrease in pore numbers. We tested this prediction for four nucleoporins (Nup98, Sec13, Nup107, and Nup153), belonging to four distinct NPC complexes, by super-resolution imaging of nuclei stained with mab414 antibody (Fig. 5 A, left). The high resolution of this data allowed us to count single NPCs accurately and compute NPC density 48 h after KD of the corresponding nucleoporin. We found that depletion of all four nucleoporins led to a significantly lower NPC density ranging from a reduction by 25% (NUP153 KD) to 60% (SEC13 KD) relative to control siRNA (Fig. 5 A, right, gray bars). For SEC13 and NUP98 KD this was in excellent agreement with the lower NPC number predicted by the model, indicating that these two phenotypes can be quantitatively explained by fewer pores in the NE. Interestingly, for NUP107 and NUP153 KD the model predicted a larger reduction in NPC density than observed experimentally. This may indicate that additional mechanisms, such as decreased permeability or a fraction of nonfunctional pores among the remaining NPCs contributes to their phenotypes.

For some genes in cluster a, the model additionally predicted a decrease in reporter stability. We also tested this prediction for NUP98 and SEC13 KD by measuring the whole cell reporter amount over time 48 h after knocking them down. In agreement with the model prediction, we found a significant decrease in total protein amount after cleavage induction compared with control siRNA (Fig. S3 D). To control that this effect was specific, we monitored total protein amount after Lamin A depletion, which, as predicted by the model, did not exhibit a difference in protein stability (Fig. S3 E).

For cluster b the model predicted a change in export rate constant (i.e., stronger or weaker binding to nuclear retention sites) as the reason for the change in accumulation of the reporter in the INM. Although a change in number of pores/permeability might also lead to change in accumulation, these two scenarios can be distinguished experimentally. To do this for the Lamin A depletion phenotype, we simulated FRAP and predicted a slower recovery in the case of decreased export (Fig. S4 A) and a faster recovery for increased pore number (Fig. S4 B). To test this prediction, we performed FRAP experiments in control siRNA and LMNA KD cells 90 min after inhibitor washout (Fig. 5 B). The recovery curves for LMNA KD cells (Fig. 5 B, red squares) show a significantly longer recovery than control siRNA-treated cells (gray circles), confirming stronger binding in the nucleus. Removal of peripheral A-type lamins might provide better access to nuclear binding sites for our LBR-based reporter, which contains binding motifs for B-type Lamins, HP1, and histone H3/H4. To test if B-type lamins are responsible for the increased accumulation after Lamin A depletion, we codepleted it with Lamin B1 and B2. Although all three lamins were significantly reduced as shown by IF staining (Fig. S4 C), reporter accumulation remained increased (Fig. 5 C), arguing that

it is not B-type lamin binding that is required. Consistent with this, knocking down lamin B1/2 alone slightly increased rather than decreased reporter accumulation (Fig. 5 C). If binding to histone H3/H4 was responsible, the N-terminally truncated reporter, containing neither binding motif, should be resistant to the Lamin A depletion phenotype. Indeed Target-INM-Δ60LBR did not show increased accumulation after LMNA KD. To test if binding to histones was responsible, we introduced a single point mutation (W16A) in the LBR nucleoplasmic domain that specifically abolishes histone binding (Hirano et al., 2012). This reporter, Target-INM-LBRW16A showed strongly reduced accumulation under control conditions (Fig. S4 D) and no longer showed an increase in INM accumulation after Lamin A depletion (Fig. 5 C). This is consistent with the report that localization of LBR depends more on chromatin than on Lamin B binding (Hirano et al., 2012).

For NUP93 in cluster c the model predicted that loss of size selectivity of the NPC was responsible for the nuclear targeting of full-length protein. To assay if the size selectivity of the NPC for soluble macromolecules was also affected, we microinjected two differently sized dextrans, normally too large to pass the NPC (70 and 160 kD; Lénárt and Ellenberg, 2006), into the cytoplasm of cells depleted of Nup93 and expressing the Target-INM-LBR reporter in the presence of the HCV protease inhibitor to prevent cleavage of the retention domain (Fig. 5 D). We selected cells that showed the Nup93 depletion phenotype of increased INM targeting for full-length Target-INM-LBR and use phenotypically negative neighboring cells as controls (Fig. 5 D, red and gray asterisks). Immediately after injection, we scored the influx of dextran into the nucleus by measuring the nuclear intensity. The nuclear concentration of 70-kD dextran was increased significantly by ~50% in KD cells compared with controls, whereas there was no statistically significant increase for the 160-kD dextran. Nup93 depletion thus appears to compromise the size selectivity of the NPC for our moderately sized membrane protein reporter, as well as for intermediate size but not for large soluble dextrans.

A Lap2β-based reporter recapitulates the LBR targeting phenotypes

To test if the general principles identified in the LBR screening are true for other INM proteins we transferred our reporter strategy to the INM protein Lap2β (Target-INM-Lap2β). Lap2β contains a single transmembrane domain and a nucleoplasmatic domain of ~40 kD that is double in size compared with LBR. Very similar to LBR, activation of the HCV protease led to Lap2β translocation from the ER to the INM and quantitative cleavage of the reporter (Fig. S4 E). We recorded Target-INM-Lap2β translocation from the ER to the INM (Fig. 6 A) and used the mathematical model to estimate the import (k_i) and export (k_o) rate constants. We found that the transport from the ER to the INM has a characteristic time of $t_{1/2} = \log(2)/k_i = 5.7–6.9$ min. We estimated a large bound fraction of Lap2β of 0.93 leading to an extremely slow export from the INM (87–103 min). Major representatives of the three phenotypic classes of genes scored in the LBR screening were then retested for also affecting Lap2β targeting. We found that Nup107-, Sec13-, Nup93-, and Lamin A–depleted cells showed a lower NE increase compared with control siRNA (Fig. 6 B). The model indicates that the four genes fall into the same phenotypic classes as for LBR (Fig. 6, C and D), i.e., the reduced accumulation at the NE after SEC13 and NUP107 KD can be accounted for by
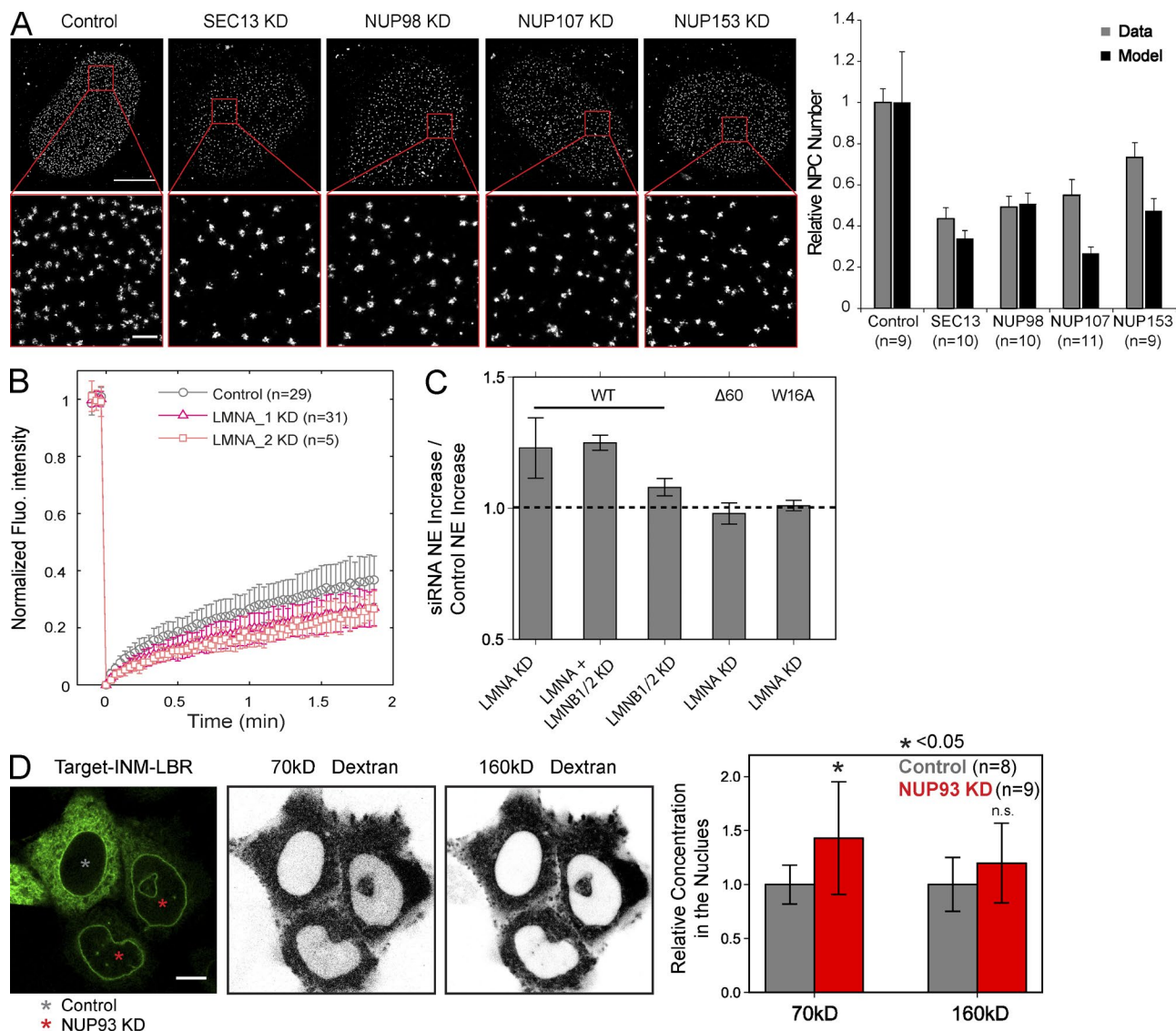
Figure 5. **Validation of model predictions.** (A, top) Super-resolved images of control siRNA and SEC13, NUP98, NUP107, and NUP153 KD nuclei stained with anti-mab414 antibody. Bar, 5 μm. (bottom) In the insets, single NPCs are visible. Bar, 500 nm. (right) NPC density derived from experimental data (gray bars) or predicted by the model (black bars) normalized to 1 relative to control siRNA. Data shown are from at least two independent experiments (n = number of cells). Error bars are the SD of the mean. (B) NE FRAP recovery curves of control siRNA (gray) and LMNA KDs (red). Data are normalized between 1 (prebleach value) and 0 (post-bleach value) and plotted over time. Data shown are from three independent experiments (LMNA_1 KD) and one replicate (LMNA_2 KD). Error bars are the SD of the mean. (C) Bar plots represent NE increase (fold change) ratio between siRNA treatment and control siRNA for Target-INM-LBR, Target-INM-LBRΔ60, and Target-INM-LBRW16A. Bars are the mean ± SD of at least three independent experiments. (D) NE permeability assay. Representative images showing, respectively, reporter (Target-INM-LBR) localization, 160- and 70-kD dextran localization in internal control (gray asterisks) or NUP93 KD cells (red asterisks). Bar, 10 μm. The bar plot shows dextran nuclear concentration relative to the control siRNA. The data shown are from a single representative experiment out of two repeats. Bars are mean ± SD.

a simultaneous reduction in import and export rates (Fig. 6 D) and the Nup93 phenotype (Fig. 6 D) by a decrease in size selectivity of the NPC. For LMNA KD (Fig. 6 D), the model predicted that changes in the binding at the INM is the underlying process explaining its effect on Lap2β targeting. In contrast to LBR, however, for Lap2β we observed a decreased accumulation and the model predicted an increased effective export rate caused by a mobilization in the INM. FRAP simulations and experiments indeed confirmed that Lap2β becomes mobilized after lamin A depletion (Fig. S4 F and Fig. 6 E).

Discussion

A general reporter system for live-cell imaging of INM protein trafficking

In this study we have established a generic strategy for live-cell imaging of INM protein translocation from the ER to the INM based on an inducible self-cleaving retention domain. We first applied this to LBR truncated after the first transmembrane domain. This reporter is effectively targeted to the INM in living cells (Ellenberg et al., 1997) and contains signals consis-
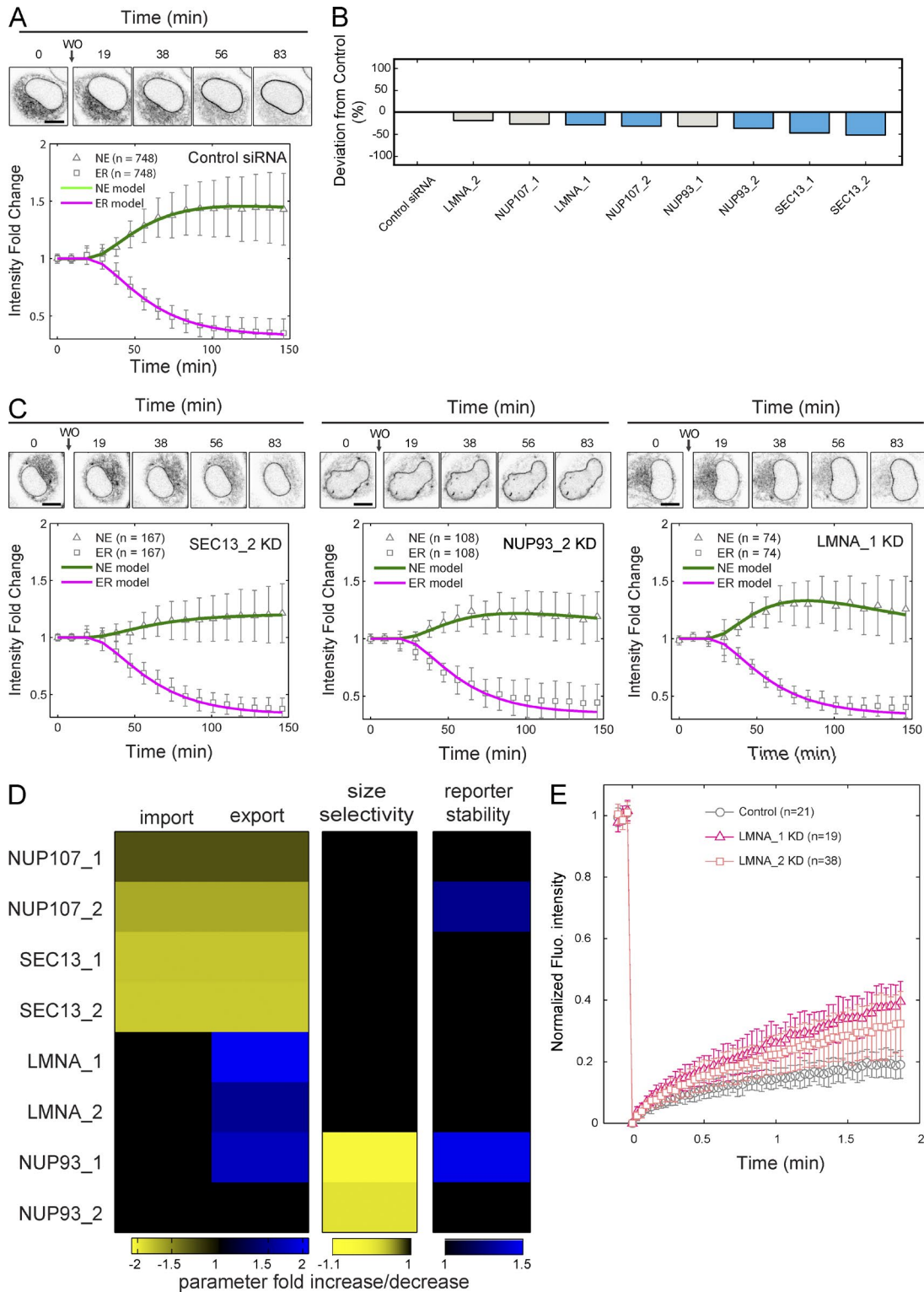
Figure 6.   **Targeting of Lap2β-based reporter.** (A) Example of single cell trajectory showing translocation of Target-INM-Lap2β reporter to the INM after inhibitor washout. Bar, 10 µm. The plots show NE and ER fold change for the control siRNA fitted by the model (solid lines). For the estimated parameters, see Table S2. (B) Ranking of NUP107, SEC13, NUP93, and LMNA siRNA based on the mean deviation of the NE increase (fold change) from control siRNA. Blue bars indicate siRNAs that deviate from control siRNA with statistical significance in at least two replicates. (C) Example of single cell trajectory and fits for SEC13_2 KD, NUP93_2 KD, and LMNA_1 KD. For the estimated parameters, Table S2. Bars, 10 µm. (D) Parameter fold changes with respect to the reference set for each of the two siRNAs of the selected four genes from the 15 hit genes. (E) NE FRAP recovery curves of control siRNA (gray) and LMNA KDs (red). Data are normalized between 1 (prebleach value) and 0 (post-bleach value) and plotted over time. Data shown are from two independent experiments (n = number of cells). Error bars are the SD of the mean.

tent with both the diffusion retention and the receptor-mediated transport model. The reporter was therefore a good starting point to screen the requirement of candidate genes in either category. We then successfully transferred the reporter strategy to Lap2β, demonstrating that its design is generic and that these two INM proteins have similar targeting requirements with the major difference being the molecular nature of their retention site. It will be very interesting to systematically compare the molecular requirements for targeting of many members of the large family of INM proteins to address if alternative pathways to diffusion retention also exist in mammalian cells.

The first siRNA screen for INM protein trafficking

siRNA screens in mammalian cells have made important contributions to map the molecular requirement of different membrane trafficking pathways (Collinet et al., 2010; Simpson et al., 2012), but our study is the first to apply this approach to INM protein targeting. The possibility to acutely release our Target-INM reporter allowed us to study ER to INM exchange kinetics directly and, in contrast to previously developed reporters (Ohba et al., 2004), we probed the behavior of the protein that binds to its physiological substrates. By systematic KD of 96 candidate genes and mathematical modeling of the resulting kinetic phenotypic signatures we could reveal which proteins are implicated in different aspects of the LBR targeting mechanism and obtain general insight about the mechanisms that normally limit INM protein targeting in living cells.

INM protein targeting is a slow process

Our combined experimental and computational approach allowed us for the first time to directly determine the exchange rate of INM proteins. For the LBR-based reporter, our data show that the efficient and specific targeting of LBR relies on an only five-fold difference in exchange rates with import characteristic time of 4–5 min and export time of 19–25 min. Based on the LBR import rate we derived that INM targeting is a comparatively slow process, with a 500 times slower transport rate compared with a completely unhindered diffusion through a membrane pore of the size of the NPC (see Materials and methods and Eq. 6), indicating that the NPC could impose a barrier to diffusive INM protein targeting. Indeed, we observed an ∼30% decrease in the import rate of Lap2β compared with LBR, consistent with the differences in size of their nucleoplasmic domains. Assuming an effective cytoplasmic concentration of 1 μM (∼2.6×10^6 molecules), the transport rate would be 4.6 molecules/NPC/min (for LBR). This rate is 30 times slower than the transport rate obtained for a freely diffusible GFP at 1 μM, consistent with a 20–100 times faster diffusion compared with integral membrane proteins (Ribbeck and Görlich, 2001; Mohr et al., 2009).

INM protein targeting sensitively depends on the number of NPCs

As discussed in this paper, NPC translocation likely represents a limiting step in INM protein targeting. This would suggest that the targeting of INM proteins depends heavily on the number of available NPCs. Indeed, the predominant protein family scoring in our LBR siRNA screen were nucleoporins, and the major predicted and validated mechanism underlying their depletion phenotype was a reduction of NPC number. This is consistent with their previously demonstrated function in NPC assembly (e.g., Nup107 and Nup98; Walther et al., 2003; Krull

et al., 2004), and in two cases (Sec13 and Nup98) we could explain their kinetic effect quantitatively.

INM protein targeting is limited by access to nuclear retention sites

Once INM proteins have reached the nucleus after passage through the pore, they can interact with nuclear binding partners, which will prevent their return to the ER. It is often assumed that nuclear binding sites are available in vast excess to INM protein ligands. In contrast, our data suggests that efficient LBR retention is normally limited because of shielding of nuclear binding sites by the peripheral lamina that lies between the INM and chromatin. Consistent with a previous study (Hirano et al., 2012), we found that LBR retention relies mostly on chromatin binding through histone H3 and is therefore increased by removal of A- or B-type lamins. The Lap2β-based reporter, in contrast, appears to be efficiently retained by interaction with lamins themselves and responded with a decrease in accumulation and mobilization in the INM to their depletion. For both INM proteins, our results suggest that the effective concentration of cognate nuclear binding sites is the second major determinant for INM protein targeting.

The Nup93-based complexes act as size controllers of the NPC for membrane proteins

Our screen revealed a third general insight, which is what controls the size selectivity of the NPC for membrane proteins. Nup93 was required to exclude the uncleaved reporter with the large retention domain in the ER, suggesting that Nup93 is part of the sizing mechanism of the NPC. It is known that Nup93 can form two distinct complexes, either with Nup188 or Nup205 (Theerthagiri et al., 2010). In our screen, NUP205 KD showed a similar phenotype as NUP93 KD, albeit with only one siRNA, whereas neither of the two NUP188 siRNAs led to loss of size selectivity against the uncleaved reporter (Fig. S4 G). Nevertheless, Nup188 likely plays a similar role because depletion from mammalian cell allows targeting of the INM protein Sun2 with an artificially enlarged nucleoplasmic domain that normally excludes it from the nucleus (Antonin et al., 2011). Together these studies suggest that different Nup93-based complexes work together to establish the NPC's size selectivity for membrane proteins.

Size selectivity for membrane and soluble proteins involves Nup93 but is likely controlled by distinct mechanisms

Nup93 depletion also led to a moderate loss of size exclusion against medium-sized soluble dextrans, suggesting that the diffusion barrier for membrane and soluble macromolecules may have the same molecular basis. This double effect is consistent with a previous study in *Caenorhabditis elegans* (Galy et al., 2003) and could be explained by the loss of the central channel Nup62 after depletion of Nup93 observed in *Xenopus leavis* extracts (Sachdev et al., 2012). However, although both soluble and membrane protein size selectivity require Nup93, they are probably mechanistically distinct because neither KD of Nup62 nor of the other major soluble diffusion barrier determinant, Nup98, affected size selectivity of the NPC in our screen, and conversely depletion of Nup188 did not impair the soluble protein diffusion barrier (Theerthagiri et al., 2010). Collectively, Nup93 is likely required for two distinct size control mecha-

nisms in the NPC, one for membrane proteins based on Nup188 and Nup205 and one for soluble proteins based on Nup62 and potentially Nup98. This would be consistent with the concept that membrane proteins pass the NPC through a route with a different size control mechanism than soluble cargo, such as the long proposed lateral channel of the NPC.

The diffusion retention model is sufficient to explain our data

As explained above, the phenotypes we observed in our screen can almost completely be explained with a diffusion retention model of INM protein targeting. For the vast majority of the genes, asymmetric effects on import or export rates were not significantly better than concomitant changes in the import and export rates. In addition, none of the KDs of 17 members of the importin α/β family affected Target-INM-LBR targeting, including importin α-16 (KPNA4-16), which has been suggested to support LBR INM targeting (Braunagel et al., 2007), although the on-target efficiency of our siRNA library was very high (Fig. S2 C). Furthermore, the strong targeting defect of Target-INM-Δ60LBR, whose active transport signals are intact, supports the idea that active transport is not sufficient to target at least LBR-based reporters. The sole exception from this rule was importin β1 (KPNB1), which showed a mild reduction in reporter accumulation. However, based on the kinetic signature of the importin β1 phenotype, our mathematical model predicts it to be caused by an increased export of the reporter rather than a decreased import, suggesting that importin β1 normally promotes retention once a membrane protein has reached the nucleus.

Materials and methods

Target-INM cloning

CMPK was isolated by PCR from *Galus Galus* CMPK-cLBR (Soullam and Worman, 1995) and cloned into hLBR1TM(1–238)-EGFP (Ellenberg et al., 1997) to generate CMPK-hLBR1TM-EGFP. To clone CMPK-NS5a/b-hLBR1TM-EGFP, NS5a/b cleavage site generated by oligo annealing was inserted into CMPK-hLBR1TM-EGFP. NS3 protease was isolated from BABA-IGZ-NS3/4a (Bartenschlager laboratory, University Heidelberg, Heidelberg, Germany) and cloned at the N terminus of CMPK-hLBR1TM-EGFP to generate NS3-CMPK-hLBR1TM-EGFP. NS3-CMPK-hLBR1TM was subcloned into pmEGFP-N1 (Takara Bio Inc.) to generate NS3-CMPK-hLBR1TM-mEGFP. NS3-CMPK-Δ60hLBR1TM-mEGFP was cloned by deletion of the first 60 aa of hLBR. W16A mutation in was introduced in NS3-CMPK-hLBR1TM-mEGFP QuikChange II Mutagenis kit (Agilent Technologies) with prime 5′-TGGTGAAGTGGTAA-GAGGTCGAGCGCCTGGGAGTTC-3′ and 5′-GAACTCCCAGGC-GCTCGACCTCTTACCACTTCACCA-3′. *Rattus Norvegicus* Lap2β (Beaudouin et al., 2002) was cloned in BamHI and AgeI replacing LBR inside NS3-CMPK-hLBR1TM-mEGFP. All constructs were inserted into pcDNA5/FRT/TO vector (Invitrogen). Transgene expression in hLBR1TM(1–238)-EGFP, pmEGFP-N1, and pcDNA5/FRT/TO constructs is driven by CMV promoter.

Cell lines

HeLa R19 FlpIn TREx allows single integration of a transgene and its inducible expression under the control of a CMV promoter (Gromeier laboratory, Duke University Medical Center, Durham, NC; Kaiser et al., 2008). Cells were grown in Dulbecco's modified Eagle's medium containing 10% fetal bovine serum, 2 mM glutamine, 1 mM sodium pyruvate, and 100 µg/ml penicillin and streptomycin. H2B-mCherry was transfected into Hela R19 FlpIn TREx with JetPrime (Polyplus Transfection) according to the protocol of the manufacturer. A clone stably expressing H2B-mCherry was isolated by selection with 0.5 µg/ml Puromycin (EMD Millipore). NS3-CMPK-hLBR1TM-mEGFP and NS3-CMPK-Δ60hLBR1TM-mEGFP pcDNA5/FRT/TO were cotransfected in the HeLa R19 FlpIn TREx/H2B-Cherry clone together with the Flp recombinase. Cells were kept under selection with 10 µg/ml Blasticidin (InvivoGen) and 200 µg/ml Hygromycin B (Invitrogen) until resistant clones were isolated.

RNAi

siRNA-spotted microarrays were generated as previously described (Erfle et al., 2008) in a 1-well LabTEK (Thermo Fisher Scientific). In brief, the transfection mix was prepared by combining 0.4 M sucrose/Opti-MEM (Life Technologies), Lipofectamine 2000 (Life Technologies) diluted 1:2 in ddH₂0, and 3 µM siRNA at 1.7:1:2.8 ratio and incubated for 20 min at room temperature in a 384-well plate (Thermo Fisher Scientific). Each siRNA transfection mix was then robotic spotted on the LabTEK surface by the VersArray_ChipWriterProSystem (Bio-Rad Laboratories). siRNAs (Silencer Select siRNA; Life Technologies) used in the screen are listed in Table S3. For total cell fluorescence, imaging cells were seeded on siRNA-coated "ready-to-transfect" 8-well LabTEK (Thermo Fisher Scientific) as described previously (Neumann et al., 2010). In brief, the transfection mix was prepared by combining 0.4 M sucrose/Opti-MEM (Life Technologies), Lipofectamine 2000 diluted 1:2 in ddH₂0, and 3 µM siRNA at 1.7:1:2.8 ratio and incubated for 20 min at room temperature. The reagents were then mixed with 0.2% gelatin at 1:0.6 ratio. The transfection mix was then diluted 1:50 in ddH₂0 and 100 µl were distributed in each well. The LabTEK were immediately dried in miVac vacuum concentrator (GeneVac, Ltd.) and stored in sealed boxes with drying pearls. For microinjection experiments, liquid siRNA transfection was done using Lipofectamine 2000 according to the protocol of the manufacturer.

Automatic time-lapse imaging

For the screening assay, the Target-INM-LBR cell line was seeded on the siRNA microarray; 24 h later, the expression of the reporter was induced with 1 µg/ml Doxycycline (Sigma-Aldrich) in the presence of 2 µM BILN2061 NS3 protease inhibitor (Boehringer Ingelheim). After an additional 24 h, we washed out the protease inhibitor and started live-cell confocal time-lapse imaging time-lapse microscopy. Each siRNA microarray was acquired with the ZEN 2010 software on a confocal microscope (LSM 780; Carl Zeiss) with a 63× Plan Apochromat oil objective, NA 1.4 (Carl Zeiss). Each siRNA spot was imaged every 9 min before inhibitor washout (two time points) and up to a 2.5 h after washout. Given that the washout occurs simultaneously for all the siRNA positions, we minimized systematic error caused by time acquisition differences by random placement of control siRNA and the two replicates of each gene targeting siRNA inside the microarray. For total cell fluorescence imaging, ZEN 2010 software on the confocal microscope with a 20× Plan Apochromat dry objective, NA 0.8 (Carl Zeiss), was used; each position was imaged every 20 min. All live-cell imaging was performed at 37°C using CO₂-independent medium without phenol red (Invitrogen) containing 20% fetal bovine serum, 2 mM L-glutamine, and 100 mg/ml penicillin and streptomycin.

Image analysis

H2B-mCherry signal was used to monitor the cell cycle stage of single cells. For this purpose, nuclei were detected in the H2B-mCherry

channel and classified with CellCognition (Held et al., 2010; Walter et al., 2010) in two morphological classes: interphase and mitotic. Cells were tracked with a constrained nearest-neighbor tracking procedure, and cell trajectories that persisted in interphase for the duration of the time-lapse were extracted. To reduce the effect of classification errors, classification results were corrected with Hidden Markov Models (Held et al., 2010; Walter et al., 2010). Target-INM reporter fluorescence intensity along each single cell trajectory was quantified in the ER and NE with an in-house developed routine implemented in MatLab. H2B-mCherry signal is used to trace the border of the nucleus, along which the NE is unfolded. The NE was divided in multiple segments with a fixed step length extending from the nucleus into the cytoplasm. Mean intensity of the Target-INM reporter was then calculated along each segment length (Fig. S2 A, 1 and 2). The first derivative of segment mean intensity in the direction from nucleus to cytoplasm was then computed; the derivative maxima (d_{max}) defines the nucleus-to-cytoplasm transition where the NE is positioned (Fig. S2 A, 2). Segments with d_{max} below a fixed intensity threshold were removed from the analysis. For the remaining segments, the position of d_{max} (Y_{max}) was used as the coordinate for deriving the following parameters: NE_{max} = highest intensity pixel in region [Y_{max}, Y_{max} + 4] (Fig. S2 A, 4); NE_{mean} = mean intensity in region [Y_{max}, Y_{max} + 4] (Fig. S2 A, 4); $Nucleus_{mean}$ = mean intensity of pixels in [Y_{max} − 6, Y_{max} − 2].

The ratio $Nucleus_{mean}/NE_{mean}$ of a segment must be below 0.6, otherwise the segment was removed from the analysis. The NE intensity was computed by averaging NE_{max} of all remaining segments. For calculating the ER intensity, we accepted as valid all the segments. We then computed a moving mean of pixels with window size equal to 1/4 of the total segments and with step size equal to one segment in the region [Y_{max} + 8, Y_{max} + 25]. Among all the computed means the highest one was selected as single value for the ER (Fig. S2 A, 5).

For the total Target-INM fluorescence measurements (Fig. S4, A and B) we used the H2B-mCherry signal and CellCognition to automatically select and track nuclei that persist in interphase for the 2.5 h of the imaging after washout. The ER was detected by thresholding the Target-INM GFP signal and single cells were separated by marker-based watershed segmentation, using the nuclei as markers. For this we used an in-house written script in FIJI (Schindelin et al., 2012) and MatLab (WholeCellQuantification.zip file in the online supplemental material). The GFP intensity for each cell is then averaged in space at every time point and the ratio is computed with respect to the first pre-washout time point.

Data analysis

For each siRNA microarray, NE and ER intensity data of single cell trajectory data were analyzed using an in-house written Python pipeline. A fixed intensity threshold was applied to remove low reporter expressing cells. For each remaining cell, raw NE and ER intensity values were normalized to the mean of the two pre-washout intensity values. The NE increase (fold change) was defined as the mean of the three highest normalized values after washout. A mean NE increase (fold change) was derived for control siRNA and gene siRNA by combining, respectively, cells from six control siRNA and two siRNA spots. Deviation of each siRNA from the control siRNA NE increase (fold change) was computed and tested for statistical significance with Student's t test (P < 0.01). For making value comparable between replicates, a percentage of NE increase (fold change) deviation from control siRNA was calculated and a combined mean deviation for the siRNA replicates was derived. The source code for the image and data analysis, including example images, can be found in the online supplemental material (Image_and_Data_Analysis.zip).

Western blotting

Cells were resuspended in ice-cold lysis buffer (10 mM Tris-Cl, pH 7.5, 150 mM, NaCl, 0.1% SDS, and 1% Triton X-100), supplemented with complete protease inhibitor cocktail and PhosSTOP phosphatase inhibitor cocktail (Roche). After 30-min incubation on rotor on ice, cells were centrifuged and the supernatants were collected. Cell lysates were loaded into NuPAGE 4–12% Bis-Tris Mini Gels (Invitrogen). The following antibodies were used for Western blotting: anti-GFP (mouse, clones 7.1/13.1; Roche); anti-Rcc1 (rabbit; Mattaj laboratory, European Molecular Biology laboratory, Heidelberg, Germany); anti-Lem4 59–938 aa (rabbit; Mattaj laboratory). Secondary antibodies used were as follows: goat anti–mouse Alexa 680 (Molecular Probes), goat anti–rabbit Alexa 680 (Molecular Probes), goat anti–mouse IRDye800CW (LI-COR Biosciences; 1:10,000), and goat anti–rabbit IRDye800CW (LI-COR Biosciences; 1:10,000). Blots were scanned in an Odyssey fluorescence imaging system (LI-COR Biosciences).

Immunofluorescence and NPC super-resolution imaging

Cells were grown for 48 h in a siRNA ready-to-transfect 8-well LabTEK. Cells were then rinsed with PBS and preextracted with 0.1% Triton X-100 (Sigma-Aldrich) and then fixed for 15 min in 2% PFA (Electron Microscopy Sciences). After extensive wash with PBS, cells were blocked with 5% normal goat serum (Life Technologies) in PBS for 1 h and incubated overnight at 4°C with primary antibody mouse mab414 1:2,500 (Covance) and then with secondary antibody 1:1,000 anti-mouse Fab Alexa Fluor 647 (Invitrogen) for 1 h at RT. The sample was embedded in GLOX-MEA buffer and imaged in a super-resolved ground state depletion microscope (Leica) with HCX Plan Apochromat 100×, NA 1.47, Oil CORR TIRF PIFOC objective (Leica) as previously described (Szymborska et al., 2013). NPC counting was done using an in-house custom written MatLab routine (NPCcount.zip file in the online supplemental material). In brief, super-resolved images were median filtered and single NPC clusters were detected. A peak detection algorithm was applied on the super-resolved raw images and the number of peaks inside each NPC cluster was counted. To define an NPC as fully assembled, a minimum of three peaks were required. NPC clusters that fulfilled this requirement were counted and a mean NPC density was computed.

Dextrans microinjection

Cells were grown overnight in a 2-well LabTEK. The next day, cells were liquid transfected with NUP93 siRNA and incubated for an additional 48 h. Microinjection was performed under a confocal microscope with a 63× Plan Apochromat oil objective, NA 1.4 (Carl Zeiss), equipped with a microinjection system (Eppendorf). Cells were microinjected with a mix of 160 kD Dextran-TRIC (Sigma-Aldrich) and 70 kD Dextran-Cy5 (Molecular Probes) in water. After 10-min equilibration, cells were imaged. Dextran intensities in the nucleus and cytoplasm were measured.

Photobleaching experiments

Cells were grown overnight for 48 h in a siRNA ready-to-transfect 8-well LabTEK. Photobleaching experiments were performed in a confocal microscope with a 63× Plan Apochromat oil objective, NA 1.4 (Carl Zeiss). Three prebleach images were acquired before bleaching. An NE region was then bleached with full laser intensity. Fluorescence recovery was followed every 2 s for a total time of 2 min. Intensity values were normalized between 1 (prebleach) and 0 (post-bleach) after correction for acquisition photobleaching using a reference cell.

Mathematical modeling

During translocation we do not observe gradients of the reporter radially away from the nucleus and the diffusion of the reporter in the ER is fast compared with the translocation time. We estimated 5 to 15 s to diffuse from the ER to the NE ($t_{1/2}$ FRAP = 20 s [Fig. S1 A] and D = 0.03–0.1 μm²/s [Zuleger et al., 2011]), whereas protein cleavage and translocation times are in the order of tens of minutes (Fig. 2 and Fig. S3, A and B). Furthermore, translocation occurs through nuclear pores evenly distributed on the NE (Fig. 5 A). We therefore assumed that in the ER, ONM, and INM the reporter density is spatially homogeneous. Finally, we assumed that chromatin and nuclear proteins retaining the reporter are in vast excess and that the binding reaction is fast so that we could perform a quasi-steady-state approximation for the binding. We thus have effective transport rates that are proportional to the number of pores N, permeabilities for import and export (P_i and P_o, respectively), and the degree of binding to nuclear proteins, calculated using:

$$k_i = NP_i \tag{1}$$

and

$$k_o = \frac{NP_o}{\beta}. \tag{2}$$

The parameter $1/\beta = (1 + K_b L)^{-1}$, where K_b is the binding constant to nuclear proteins and L their concentration, gives the fraction of free reporter at the INM. The fraction of reporter bound to nuclear proteins is given by

$$f_b = \frac{\beta - 1}{\beta}. \tag{3}$$

For a pure diffusive transport we expect $P_i = P_o = P$. In this case, to vary the number of pores and/or permeability compared with the control dataset we change k_i and k_o but leave the ratio equal to the ratio obtained for control.

The effective export rate constant (Eq. 2) is derived by first expressing the time changes of the bound C_b and free reporter density $\overline{C}_{INM}$ at the INM:

$$\frac{dC_b}{dt} = k_b L \overline{C}_{INM} - k_{-b} C_b - d_{CINM} C_b$$

and

$$\frac{d\overline{C}_{INM}}{dt} = k_i C_{ONM} - \overline{k}_o \overline{C}_{INM} - k_b L \overline{C}_{INM} + k_{-b} C_b - d_{CINM} \overline{C}_{INM}.$$

$\overline{k}_o = NP_o$ is the export rate of the free protein, C_{ONM} is the density of the cleaved form in the ONM, k_b and k_{-b} are the binding and unbinding rate constants, and L is the concentration of binding sites. We found that from the FRAP and targeting kinetics we only obtain a lower value for k_{-b} >0.25/min (95% confidence interval estimated using the profile-likelihood method). Assuming fast binding $k_b L, k_{-b} \gg d_{CINM}$ we obtain $C_b \approx \frac{k_b L}{k_{-b}} \overline{C}_{INM}$ and so $\overline{C}_{INM} = \frac{C_{INM}}{1 + K_b L} = \frac{C_{INM}}{\beta}$, where the total cleaved density in the INM is $C_{INM} = C_b + \overline{C}_{INM}$. The ordinary differential equation for the total density is then given by the following equation:

$$\frac{dC_{INM}}{dt} = k_i C_{ONM} - k_o C_{INM} - d_{CINM} C_{INM},$$

with the effective export rate constant k_o defined in Eq. 2. The quasi-steady-state approximation slightly underestimates the value for the import and export rate constants. However, we found that for binding reactions equilibrating within 4 min (the maximal possible range) the difference is <10%.

We define the total density of full-length and cleaved protein in the ER and ONM, computed with respect to the ER area, by F = $F_{ER} + F_{ONM}/\alpha$ and $C = C_{ER} + C_{ONM}/\alpha$, respectively. The subscripts indicate the localization of the reporter. The parameter $\alpha = A_{ER}/A_{INM}$ gives the area ratio of the membranes. The system of ordinary differential equations reads as follows:

$$\frac{dF}{dt} = v_t \frac{(\alpha + 1)}{\alpha} - \left(k_c + d_F + \frac{\lambda k_i}{1 + \alpha} \right) F + \frac{\lambda k_o}{\alpha} F_{INM},$$

$$\frac{dC}{dt} = k_c F - \left(d_C + \frac{k_i}{1 + \alpha} \right) C + \frac{k_o}{\alpha} C_{INM},$$

$$\frac{dC_{INM}}{dt} = k_c F_{INM} + \frac{\alpha k_i}{1 + \alpha} C - (d_{CINM} + k_o) C_{INM},$$

and

$$\frac{dF_{INM}}{dt} = \frac{\alpha \lambda k_i}{1 + \alpha} F - (d_F + k_c + \lambda k_o) F_{INM}.$$

The parameter $1 - \lambda$ characterizes the size selectivity barrier of the pore; a value of 0 indicates that the full-length protein can equally translocate through the pore as the smaller cleaved protein. The experimentally observables quantities in the ER and NE are a linear combination of these variables:

$$ER = (F + C) \frac{\alpha}{1 + \alpha} \tag{4}$$

and

$$NE = (F + C) \frac{\alpha}{1 + \alpha} + C_{IN} + F_{IN}. \tag{5}$$

These quantities, normalized to their initial steady-state values (at $t = 0$), are used to fit experimental data. The total reporter density, for $d_C = d_{CINM}$ and computed with respect to ER area, is given by:

$$\frac{dF_{tot}}{dt} = v_t \frac{(\alpha + 1)}{\alpha} - \left(k_c + d_F \right) F_{tot}$$

and

$$\frac{dC_{tot}}{dt} = k_c F_{tot} - d_C C_{tot}.$$

The system of ordinary differential equations is solved analytically for $k_c = k_{cb}$ for t < 20 min and $k_c = 0.0342$ min⁻¹ for t ≥ 20 min, where k_{cb} is a small basal cleavage rate constant.

FRAP simulations

We simulated FRAP on a simplified 1D circular geometry representing the nuclear rim. In experiments, the length of the bleached NE segment is 6–7 μm and the perimeter of nuclei is ~70 μm. We simulated a 70-μm-long NE and a bleached size of 7 μm. The diffusion in the INM is characterized by an effective diffusion coefficient, $D_{eff} = D/\beta$. The free diffusion coefficient D, i.e., in the absence of binding, has been estimated by simultaneously fitting the FRAP and targeting kinetics of Target-INM-LBR and Target-INM-Lap2β for the control siRNA, assuming an equal diffusion coefficient for both proteins. We found that a value of D = 0.15–0.35 μm²/s could reproduce the targeting and FRAP data. In all the FRAP simulations, a value of D = 0.2 μm²/s has been taken.

Model parameter estimation

For parameter estimation we minimized the mean squared distance of the model to the normalized NE and ER densities and the initial ($t = 0$) ER to NE density ratio. We first determined reference parameter sets

for LBR and Lap2β with control siRNA. For Lap2β, and to a lesser extent for LBR, we found that the export rate constant was only poorly determined by the targeting data. To better constrain this parameter we also simultaneously fitted the FRAP curves for the control siRNA. For Lap2β we could find a significant improvement in the fits assuming $d_C \neq d_{CINM}$ and $k_{cb} > 0$; for LBR we kept $d_C = d_{CINM}$ and $k_{cb} = 0$. For both targeting constructs $\lambda > 0$ did not improve the fits for the control siRNA.

For simulating the targeting for siRNA KD, we searched for the minimal set of parameters different from control. We tested 20 parameter combinations using cross-validation (Fig. S3 G) and proceeded as follows: using resampling without replacing we generated a dataset of maximally 30 cells and split it into two; in the cross-validation step we fit the 20 parameter combinations to one half of the data and computed the predicted χ^2 for the other half; we repeated this procedure 100 times and compared pairs of parameter combinations with a Kolmogorov-Smirnov test (P < 0.01).

We chose the smallest parameter combination if the statistical test was not significant. If sets changing NP (leaving the ratio of k_i and k_o unchanged), k_i, or k_o were not statistically different we chose sets changing NP. The rationale is that, for a pure diffusive transport, a change in number of pores and/or permeability after KD is more likely than a unidirectional change of one of the rates. If sets changing k_i or k_o were not statistically different, we took the sets with the smallest predicted χ^2.

To estimate the confidence intervals we used bootstrapping and repeated the fitting for 100 resampled datasets. These sets are obtained from the original datasets by resampling with replacing and contain the same number of cells as the original dataset.

Estimating transport rates per NPC

The maximal transport rate through a single membrane pore of radius $R = 60$ nm and length $L = 40$ nm (Maimon et al., 2012) is derived from Fick's first law:

$$f_{max} = \frac{D\pi R\Delta C N_A}{L}(1 - r/R)^2,$$

where D is the membrane diffusion of the reporter, r is the hydrodynamic radius of the cytoplasmic moiety, and ΔC is the concentration difference between INM and ONM. The last term describes steric hindrance of entry into the channel (Mohr et al., 2009). For the transport rate estimated from our kinetic model we have

$$f_{exp} = \frac{\alpha}{1+\alpha}\frac{k_i C A_{NM} N_A}{N} = \frac{\alpha}{1+\alpha}\frac{k_i C N_A}{\rho_{NPC}},$$

where ρ_{NPC} is the density of nuclear pores, here estimated to be ∼9 NPC/μm² (Fig. 5). At washout, the density in INM is ∼0, therefore $\Delta C = C$. We can then compute the ratio of these two rates, which is independent of concentrations, as

$$\frac{f_{max}}{f_{exp}} = \frac{1+\alpha}{\alpha}\frac{DR\pi\rho_{NPC}}{k_i L}(1 - r/R)^2. \quad (6)$$

To compare the absolute transport rates obtained here to previous reported rates for diffusible proteins at a standard cytoplasmic concentration of 1 μM (Ribbeck and Görlich, 2001; Mohr et al., 2009), we need to convert the concentration to a surface density. In the cell line used in this study we estimated from fluorescent images the area ratio of ER and nuclear membrane as

$$\alpha = \frac{A_{ER}}{A_{NM}} = 7,$$

a nuclear membrane area of 1,200 μm², and a cytoplasmic volume (including ER and organelles) of 4,650 μm³ (Fig. S3). This yields a surface area ER density of ∼2 μm²/μm³. From this we can compute, assuming evenly distributed ER, that a 1 μM "concentration" corresponds to an ER surface density of 5×10^{-22} mol/μm².

Online supplemental material

Fig. S1 proves INM localization of LBR and Lap2β reporters by FRAP and IF after Triton/Digitonin permeabilization. Fig. S2 illustrates image analysis pipeline and validation of siRNA KD efficiency. Fig. S3 shows model parameter estimation. Fig. S4 contains FRAP simulation for LBR and Target-INM-LBRW16A and Target-INM-Lap2β validation. Table S1 contains parameters values for Target-INM-LBR. Table S2 contains parameters values Target-INM-Lap2β. Table S3 contains a list of siRNAs used in the screen. Table S4 contains the ranking of siRNA based on NE increase (fold change). The source code for the image and data analysis methods can be found online. *ER_NE ratio* contains the code for calculating ER/NE ratio (Fig. S3 C). *Image_and_Data_Analysis* contains the source code for image and data analysis of the screen data. *WholeCellQuantification* contains the source code for calculating whole cell intensity in 20× data (Fig. S3, D and E). *NPCcount* contains the source code for NPC counting (Fig. 5 A). Online supplemental material is available at http://www.jcb.org/cgi/content/full/jcb.201409133/DC1.

References

Antonin, W., R. Ungricht, and U. Kutay. 2011. Traversing the NPC along the pore membrane: targeting of membrane proteins to the INM. *Nucleus.* 2:87–91. http://dx.doi.org/10.4161/nucl.2.2.14637

Beaudouin, J., D. Gerlich, N. Daigle, R. Eils, and J. Ellenberg. 2002. Nuclear envelope breakdown proceeds by microtubule-induced tearing of the lamina. *Cell.* 108:83–96. http://dx.doi.org/10.1016/S0092-8674(01)00627-4

Beck, M., F. Förster, M. Ecke, J.M. Plitzko, F. Melchior, G. Gerisch, W. Baumeister, and O. Medalia. 2004. Nuclear pore complex structure and dynamics revealed by cryoelectron tomography. *Science.* 306:1387–1390. http://dx.doi.org/10.1126/science.1104808

Braunagel, S.C., S.T. Williamson, S. Saksena, Z. Zhong, W.K. Russell, D.H. Russell, and M.D. Summers. 2004. Trafficking of ODV-E66 is mediated via a sorting motif and other viral proteins: facilitated trafficking to the inner nuclear membrane. *Proc. Natl. Acad. Sci. USA.* 101:8372–8377. http://dx.doi.org/10.1073/pnas.0402727101

Braunagel, S.C., S.T. Williamson, Q. Ding, X. Wu, and M.D. Summers. 2007. Early sorting of inner nuclear membrane proteins is conserved. *Proc. Natl. Acad. Sci. USA.* 104:9307–9312. http://dx.doi.org/10.1073/pnas.0703186104

Braunagel, S.C., V. Cox, and M.D. Summers. 2009. Baculovirus data suggest a common but multifaceted pathway for sorting proteins to the inner nuclear membrane. *J. Virol.* 83:1280–1288. http://dx.doi.org/10.1128/JVI.01661-08

Burke, B., and C.L. Stewart. 2006. The laminopathies: the functional architecture of the nucleus and its contribution to disease. *Annu. Rev. Genomics Hum. Genet.* 7:369–405. http://dx.doi.org/10.1146/annurev.genom.7.080505.115732

Collinet, C., M. Stöter, C.R. Bradshaw, N. Samusik, J.C. Rink, D. Kenski, B. Habermann, F. Buchholz, R. Henschel, M.S. Mueller, et al. 2010. Systems survey of endocytosis by multiparametric image analysis. *Nature.* 464:243–249. http://dx.doi.org/10.1038/nature08779

Ellenberg, J., E.D. Siggia, J.E. Moreira, C.L. Smith, J.F. Presley, H.J. Worman, and J. Lippincott-Schwartz. 1997. Nuclear membrane dynamics and reassembly in living cells: targeting of an inner nuclear membrane protein in interphase and mitosis. *J. Cell Biol.* 138:1193–1206. http://dx.doi.org/10.1083/jcb.138.6.1193

Erfle, H., B. Neumann, P. Rogers, J. Bulkescher, J. Ellenberg, and R. Pepperkok. 2008. Work flow for multiplexing siRNA assays by solid-phase reverse transfection in multiwell plates. *J. Biomol. Screen.* 13:575–580. http://dx.doi.org/10.1177/1087057108320133

Galy, V., I.W. Mattaj, and P. Askjaer. 2003. *Caenorhabditis elegans* nucleoporins Nup93 and Nup205 determine the limit of nuclear pore complex size exclusion in vivo. *Mol. Biol. Cell.* 14:5104–5115. http://dx.doi.org/10.1091/mbc.E03-04-0237

Gardner, J.M., C.J. Smoyer, E.S. Stensrud, R. Alexander, M. Gogol, W. Wiegraebe, and S.L. Jaspersen. 2011. Targeting of the SUN protein Mps3 to the inner nuclear membrane by the histone variant H2A.Z. *J. Cell Biol.* 193:489–507. http://dx.doi.org/10.1083/jcb.201011017

Gomez-Cavazos, J.S., and M.W. Hetzer. 2012. Outfits for different occasions: tissue-specific roles of Nuclear Envelope proteins. *Curr. Opin. Cell Biol.* 24:775–783. http://dx.doi.org/10.1016/j.ceb.2012.08.008

Held, M., M.H.A. Schmitz, B. Fischer, T. Walter, B. Neumann, M.H. Olma, M. Peter, J. Ellenberg, and D.W. Gerlich. 2010. CellCognition: time-resolved phenotype annotation in high-throughput live cell imaging. *Nat. Methods.* 7:747–754. http://dx.doi.org/10.1038/nmeth.1486

Hirano, Y., K. Hizume, H. Kimura, K. Takeyasu, T. Haraguchi, and Y. Hiraoka. 2012. Lamin B receptor recognizes specific modifications of histone H4 in heterochromatin formation. *J. Biol. Chem.* 287:42654–42663. http://dx.doi.org/10.1074/jbc.M112.397950

Kaiser, C., E.Y. Dobrikova, S.S. Bradrick, M. Shveygert, J.T. Herbert, and M. Gromeier. 2008. Activation of cap-independent translation by variant eukaryotic initiation factor 4G in vivo. *RNA.* 14:2170–2182. http://dx.doi.org/10.1261/rna.1171808

King, M.C., C.P. Lusk, and G. Blobel. 2006. Karyopherin-mediated import of integral inner nuclear membrane proteins. *Nature.* 442:1003–1007. http://dx.doi.org/10.1038/nature05075

Krull, S., J. Thyberg, B. Björkroth, H.R. Rackwitz, and V.C. Cordes. 2004. Nucleoporins as components of the nuclear pore complex core structure and Tpr as the architectural element of the nuclear basket. *Mol. Biol. Cell.* 15:4261–4277. http://dx.doi.org/10.1091/mbc.E04-03-0165

Lamarre, D., P.C. Anderson, M. Bailey, P. Beaulieu, G. Bolger, P. Bonneau, M. Bös, D.R. Cameron, M. Cartier, M.G. Cordingley, et al. 2003. An NS3 protease inhibitor with antiviral effects in humans infected with hepatitis C virus. *Nature.* 426:186–189. http://dx.doi.org/10.1038/nature02099

Lénárt, P., and J. Ellenberg. 2006. Monitoring the permeability of the nuclear envelope during the cell cycle. *Methods.* 38:17–24. http://dx.doi.org/10.1016/j.ymeth.2005.07.010

Lin, M.Z., J.S. Glenn, and R.Y. Tsien. 2008. A drug-controllable tag for visualizing newly synthesized proteins in cells and whole animals. *Proc. Natl. Acad. Sci. USA.* 105:7744–7749. http://dx.doi.org/10.1073/pnas.0803060105

Lusk, C.P., G. Blobel, and M.C. King. 2007. Highway to the inner nuclear membrane: rules for the road. *Nat. Rev. Mol. Cell Biol.* 8:414–420. http://dx.doi.org/10.1038/nrm2165

Maimon, T., N. Elad, I. Dahan, and O. Medalia. 2012. The human nuclear pore complex as revealed by cryo-electron tomography. *Structure.* 20:998–1006. http://dx.doi.org/10.1016/j.str.2012.03.025

Meinema, A.C., J.K. Laba, R.A. Hapsari, R. Otten, F.A. Mulder, A. Kralt, G. van den Bogaart, C.P. Lusk, B. Poolman, and L.M. Veenhoff. 2011. Long unfolded linkers facilitate membrane protein import through the nuclear pore complex. *Science.* 333:90–93. http://dx.doi.org/10.1126/science.1205741

Mohr, D., S. Frey, T. Fischer, T. Güttler, and D. Görlich. 2009. Characterisation of the passive permeability barrier of nuclear pore complexes. *EMBO J.* 28:2541–2553. http://dx.doi.org/10.1038/emboj.2009.200

Neumann, B., T. Walter, J.K. Hériché, J. Bulkescher, H. Erfle, C. Conrad, P. Rogers, I. Poser, M. Held, U. Liebel, et al. 2010. Phenotypic profiling of the human genome by time-lapse microscopy reveals cell division genes. *Nature.* 464:721–727.

Ohba, T., E.C. Schirmer, T. Nishimoto, and L. Gerace. 2004. Energy- and temperature-dependent transport of integral proteins to the inner nuclear membrane via the nuclear pore. *J. Cell Biol.* 167:1051–1062. http://dx.doi.org/10.1083/jcb.200409149

Powell, L., and B. Burke. 1990. Internuclear exchange of an inner nuclear membrane protein (p55) in heterokaryons: in vivo evidence for the interaction of p55 with the nuclear lamina. *J. Cell Biol.* 111:2225–2234. http://dx.doi.org/10.1083/jcb.111.6.2225

Reichelt, R., A. Holzenburg, E.L. Buhle Jr., M. Jarnik, A. Engel, and U. Aebi. 1990. Correlation between structure and mass distribution of the nuclear pore complex and of distinct pore complex components. *J. Cell Biol.* 110:883–894. http://dx.doi.org/10.1083/jcb.110.4.883

Ribbeck, K., and D. Görlich. 2001. Kinetic analysis of translocation through nuclear pore complexes. *EMBO J.* 20:1320–1330. http://dx.doi.org/10.1093/emboj/20.6.1320

Sachdev, R., C. Sieverding, M. Flötenmeyer, and W. Antonin. 2012. The C-terminal domain of Nup93 is essential for assembly of the structural backbone of nuclear pore complexes. *Mol. Biol. Cell.* 23:740–749. http://dx.doi.org/10.1091/mbc.E11-09-0761

Saksena, S., Y. Shao, S.C. Braunagel, M.D. Summers, and A.E. Johnson. 2004. Cotranslational integration and initial sorting at the endoplasmic reticulum translocon of proteins destined for the inner nuclear membrane. *Proc. Natl. Acad. Sci. USA.* 101:12537–12542. http://dx.doi.org/10.1073/pnas.0404934101

Saksena, S., M.D. Summers, J.K. Burks, A.E. Johnson, and S.C. Braunagel. 2006. Importin-α-16 is a translocon-associated protein involved in sorting membrane proteins to the nuclear envelope. *Nat. Struct. Mol. Biol.* 13:500–508. http://dx.doi.org/10.1038/nsmb1098

Schindelin, J., I. Arganda-Carreras, E. Frise, V. Kaynig, M. Longair, T. Pietzsch, S. Preibisch, C. Rueden, S. Saalfeld, B. Schmid, et al. 2012. Fiji: an open-source platform for biological-image analysis. *Nat. Methods.* 9:676–682. http://dx.doi.org/10.1038/nmeth.2019

Simpson, J.C., B. Joggerst, V. Laketa, F. Verissimo, C. Cetin, H. Erfle, M.G. Bexiga, V.R. Singan, J.K. Hériché, B. Neumann, et al. 2012. Genome-wide RNAi screening identifies human proteins with a regulatory function in the early secretory pathway. *Nat. Cell Biol.* 14:764–774. http://dx.doi.org/10.1038/ncb2510

Smith, S., and G. Blobel. 1993. The first membrane spanning region of the lamin B receptor is sufficient for sorting to the inner nuclear membrane. *J. Cell Biol.* 120:631–637. http://dx.doi.org/10.1083/jcb.120.3.631

Soullam, B., and H.J. Worman. 1995. Signals and structural features involved in integral membrane protein targeting to the inner nuclear membrane. *J. Cell Biol.* 130:15–27. http://dx.doi.org/10.1083/jcb.130.1.15

Szymborska, A., A. de Marco, N. Daigle, V.C. Cordes, J.A. Briggs, and J. Ellenberg. 2013. Nuclear pore scaffold structure analyzed by super-resolution microscopy and particle averaging. *Science.* 341:655–658. http://dx.doi.org/10.1126/science.1240672

Theerthagiri, G., N. Eisenhardt, H. Schwarz, and W. Antonin. 2010. The nucleoporin Nup188 controls passage of membrane proteins across the nuclear pore complex. *J. Cell Biol.* 189:1129–1142. http://dx.doi.org/10.1083/jcb.200912045

Turgay, Y., R. Ungricht, A. Rothballer, A. Kiss, G. Csucs, P. Horvath, and U. Kutay. 2010. A classical NLS and the SUN domain contribute to the targeting of SUN2 to the inner nuclear membrane. *EMBO J.* 29:2262–2275. http://dx.doi.org/10.1038/emboj.2010.119

Walter, T., M. Held, B. Neumann, J.K. Hériché, C. Conrad, R. Pepperkok, and J. Ellenberg. 2010. Automatic identification and clustering of chromosome phenotypes in a genome wide RNAi screen by time-lapse imaging. *J. Struct. Biol.* 170:1–9. http://dx.doi.org/10.1016/j.jsb.2009.10.004

Walther, T.C., A. Alves, H. Pickersgill, I. Loïodice, M. Hetzer, V. Galy, B.B. Hülsmann, T. Köcher, M. Wilm, T. Allen, et al. 2003. The conserved Nup107-160 complex is critical for nuclear pore complex assembly. *Cell.* 113:195–206. http://dx.doi.org/10.1016/S0092-8674(03)00235-6

Yang, L., T. Guan, and L. Gerace. 1997. Integral membrane proteins of the nuclear envelope are dispersed throughout the endoplasmic reticulum during mitosis. *J. Cell Biol.* 137:1199–1210. http://dx.doi.org/10.1083/jcb.137.6.1199

Ye, Q., and H.J. Worman. 1994. Primary structure analysis and lamin B and DNA binding of human LBR, an integral protein of the nuclear envelope inner membrane. *J. Biol. Chem.* 269:11306–11311.

Zuleger, N., D.A. Kelly, A.C. Richardson, A.R. Kerr, M.W. Goldberg, A.B. Goryachev, and E.C. Schirmer. 2011. System analysis shows distinct mechanisms and common principles of nuclear envelope protein dynamics. *J. Cell Biol.* 193:109–123. http://dx.doi.org/10.1083/jcb.201009068